A 3D LBM-DEM study of sheared particle suspensions under the influence of temperature-dependent viscosity

J.W.S. McCullough[a,*], Ł. Łaniewski-Wołłk[a,b], S.M. Aminossadati[a], C.R. Leonardi[a]

[a] *The University of Queensland, School of Mechanical and Mining Engineering, Cooper Road, St Lucia QLD 4072, Australia*
[b] *Institute of Aeronautics and Applied Mechanics, Warsaw University of Technology, Warsaw 00-665, Poland*

Abstract

Particle suspensions form a fundamental yet complex component of many scientific and engineering endeavours. This paper proposes a numerical coupling between the lattice Boltzmann and discrete element methods that resolves particle suspensions exposed to thermal influences due to temperature-dependent fluid viscosity and conjugate heat transfer between components. Validation of the model was performed via the study of the relative viscosity of suspensions. This numerically corroborated the proposed temperature-dependence of the relative viscosity of suspensions. The model was finally used to interrogate the macroscopic behaviour of sheared suspensions at a range of solid volume fractions. This demonstrated changes in suspension flow behaviour due to temperature related effects. Future work based on these results would examine how particle properties could be modified to exacerbate and control temperature-based phenomena potentially leading to improvements in domains such as industrial material processing and manufacture.

Keywords: Particle suspensions, Thermal lattice Boltzmann method, Discrete element method, Temperature-dependent viscosity

*Corresponding author
Email addresses: jon.mccullough@uqconnect.edu.au (J.W.S. McCullough), l.laniewskiwollk@uq.edu.au (Ł. Łaniewski-Wołłk), s.aminossadati@uq.edu.au (S.M. Aminossadati), c.leonardi@uq.edu.au (C.R. Leonardi)

1. Introduction

In a number of applications of scientific and industrial interest, particle suspensions are used to transport heat and mass through the system. The combination of solid and fluid components enables the physical properties of each to be used to advantage during operation. The interaction of components with each other and the surrounding environment can include hydrodynamic, thermodynamic and mechanical interactions. The complexity of these, both individually and collectively, means that the study of suspensions can be difficult to perform from a completely analytical standpoint.

The study of sheared suspensions is widely used in both numerical and physical experiments to study how they behave under a variety of conditions. Physical tests are often used in this setting to evaluate fitting coefficients for a chosen empirical model. Due to fluid-particle and particle-wall interactions, the effective viscosity of a suspension increases with solid volume fraction. A number of empirical correlations for this behaviour can be found in the literature [1–5]. What can be noted from these correlations is that the behaviour of the suspension becomes more sensitive to experimental layout and material properties as the particle solid volume fraction, ϕ, increases. These correlations often examine how the effective viscosity of the suspension, μ_E, changes in comparison to the the viscosity of the base fluid. This is often expressed as a ratio, μ_R. Some correlations that can be found in the literature include the Krieger-Dougherty equation [1, 3, 6]:

$$\mu_R = \left(1 - \frac{\phi}{\phi_M}\right)^{-2.5\phi_M}; \tag{1}$$

the Eilers correlation [3, 4]:

$$\mu_R = \left(1 + \frac{1.5\phi}{1 - \frac{\phi}{\phi_M}}\right)^2; \tag{2}$$

the Mooney equation [1]:

$$\mu_R = e^{\left(\frac{2.5\phi}{1 - \frac{\phi}{\phi_M}}\right)}; \tag{3}$$

and the correlation proposed by Morris and Boulay [2, 5]:

$$\mu_R = 0.133 + I + 2.5\phi_M\sqrt{\frac{4I}{3}}; \tag{4}$$

where $I = \frac{4}{3}\left(\frac{\phi_M}{\phi} - 1\right)$. In these expressions ϕ_M is used to represent the maximum random packing fraction of spheres into a volume. A value of $\phi_M = 0.64$ is used for the Krieger-Dougherty and Mooney equations, the Eilers equation uses $\phi_M = 0.58$ while the Morris-Boulay expression takes $\phi_M = 0.68$. Although used as a model fitting parameter in these correlations, ϕ_M should ultimately be a constant geometric property.

Numerical studies of suspensions firstly allow this parameter fitting to occur using reliable and repeatable conditions for both boundary conditions and the concentration and distributions of the solid component. The use of numerical tools to study suspensions also allows macroscopic properties of suspensions to be examined to a level of detail that is generally not possible using physical studies. In contrast, physical experiments can be used to fit certain parameters but are much more sensitive to operating conditions and experimental layout. The measurement of physical properties of the suspension also needs to be performed such that it does not interfere with its natural behaviour. An advantage of such studies though is that the exact behaviour of a suspension formulation can be observed.

The lattice Boltzmann method (LBM) provides a good starting point for modelling particle suspensions as its formulation is amenable to the transient boundary movement observed between components. Modification of the LBM relaxation approach is sufficient to capture the behaviour of particles moving within the fluid. An additional benefit of this is that the base grid of LBM nodes is not required to be redistributed as the system evolves, unlike finite volume based approaches. This can reduce bottlenecks in computation. The LBM's localised approach to fluid viscosity also makes it a suitable candidate for modelling flows with temperature-dependent viscosity. Despite this, the concept has only been discussed in a relatively small number of previous works [7–10]. In some of our previous work [11], we have demonstrated that a total energy

approach for thermal flows can capture behaviour associated with temperature-dependent viscosity to second-order accuracy.

In many prior studies of particle suspensions that include thermal effects, the particles are often represented using constant temperature or constant heat flux boundary conditions [12–14]. A physically realistic boundary condition ensures that conjugate heat transfer (CHT) is maintained at the interface of fluid and solid components. This requires that both continuity of temperature: $T^{I,+} = T^{I,-}$; and heat flux: $\mathbf{n} \cdot (k\nabla T + \rho C_p \mathbf{u} T)^{I,+} = \mathbf{n} \cdot (k\nabla T + \rho C_p \mathbf{u} T)^{I,-}$; is maintained at the interface. Here, the $+$ and $-$ indicate the two sides of interface I and $\mathbf{n}$ indicates the interface normal. k, ρ and C_p are the thermal conductivity, density and heat capacity of the respective materials whilst $\mathbf{u}$ is the velocity of the medium. A number of approaches for CHT have been proposed in an LBM setting for static interfaces [15–21]. Applications in transient suspensions are less prevalent with examples including some of the authors' previous work [22–24].

This study will make use of the LBM to study some of the macroscopic properties in sheared particle suspensions possessing a fluid with temperature-dependent viscosity. The remainder of this paper consists of the following structure. Section 2 describes the numerical methods used for modelling in this research. Section 3 presents the verification of the model and the investigations conducted with it. The work is then summarised in Section 4.

2. Details of numerical modelling

In this work a coupled approach using the LBM and the discrete element method (DEM) was employed to capture the behaviour of particle suspensions. These were implemented using the open-source TCLB [25] and ESyS-Particle [26]respectively. As in a prior study [11], the total energy conserving implementation of LBM for thermal flows from Guo et al.[8] is utilised here. This approach allows for a fluid with temperature-dependent viscosity to be accurately captured using an LBM framework. Again following the strategy from

previous works [11, 22, 23] the second LBM population is used to capture the thermal behaviour of both the solid and fluid components. In this paper, the approach of Pareschi et al.[18] is implemented to allow conjugate heat transfer (CHT) to be conserved between the solid and fluid components.

2.1. Total energy LBM - Fluid and temperature

The LBM implementation proposed by Guo et al.[8] uses a two-population approach to allow resolution of fluid flows exposed to thermal influences. The first population, denoted by $f_i(\mathbf{x}, t)$ is used to capture the hydrodynamic behaviour of the fluid. In the absence of body forces acting on the fluid, this discrete density distribution function is streamed and relaxed upon a Cartesian grid with even spacings of Δx according to a single relaxation time scheme,

$$f_i(\mathbf{x} + \mathbf{e_i}\Delta t, t + \Delta t) - f_i(\mathbf{x}, t) = -\tau_f^{-1}(f_i(\mathbf{x}, t) - f_i^{eq}(\mathbf{x}, t)). \tag{5}$$

In this expression $f_i^{eq}(\mathbf{x}, t)$ is an equilibrium function that the population relaxes towards based on the relaxation time τ_f and $\mathbf{e_i}$ is the velocity vector in direction i. The equilibrium function takes the form,

$$f_i^{eq}(\mathbf{x}, t) = \omega_i \rho \left[1 + \frac{3}{c_s^2}(\mathbf{e_i} \cdot \mathbf{u}) + \frac{9}{2c_s^4}(\mathbf{e_i} \cdot \mathbf{u})^2 - \frac{3}{2c_s^2}(\mathbf{u} \cdot \mathbf{u})\right], \tag{6}$$

in which ω_i is a set of lattice-specific weights and c_s^2 is the lattice speed of sound squared that takes a value of $1/3$ in dimensionless lattice units. After a Chapman-Enskog analysis, this yields the Navier-Stokes equations for fluid flow in a low Mach number limit. This process also allows the definition of the fluid kinematic viscosity, ν, to be related to the lattice spacing, Δx, and time step, Δt, through,

$$\nu = \frac{1}{3}\left(\tau_f - \frac{1}{2}\right)\frac{(\Delta x)^2}{\Delta t}. \tag{7}$$

Here, the choice of physical values of Δx and Δt converts between viscosity in lattice ($\Delta x = \Delta t = 1$) and physical units. In this study, ν is allowed to vary locally with temperature and from this a local value for τ_f can be defined.

Macroscopic properties of interest are found by taking moments of the $f_i(\mathbf{x}, t)$ population. Subsequently, these are also dependent on both location and time.

For clarity, the '$(\mathbf{x}, t)$' notation will be implied for these terms in the remainder of the paper. In particular, this allows computation of density,

$$\rho = \sum_i f_i; \tag{8}$$

momentum,

$$\rho \mathbf{u} = \sum_i f_i \mathbf{e_i}; \tag{9}$$

and the viscous stress tensor

$$S_{\gamma\delta} = -\left(1 - 1/(2\tau_f)\right) \sum_i \mathbf{e_i}_\gamma \mathbf{e_i}_\delta (f_i - f_i^{eq}). \tag{10}$$

The quantity conserved by the second population, g_i, is total energy such that $\sum_i g_i = \rho E$. Here $E = C_p T + 0.5\,(\mathbf{u} \cdot \mathbf{u})$, C_p is the specific heat capacity of the fluid, and T is the temperature. Again in the absence of body forces on a N-dimensional lattice, the thermal population possesses an equilibrium of

$$g_i^{eq} = \omega_i \rho c_s^2 \left[\frac{\mathbf{e_i} \cdot \mathbf{u}}{c_s^2} + \left(\frac{\mathbf{e_i} \cdot \mathbf{u}}{c_s^2} \right)^2 - \frac{\mathbf{u} \cdot \mathbf{u}}{2c_s^2} + \left(\frac{\mathbf{e_i}^2}{2c_s^2} - \frac{N}{2} \right) \right] + E f_i^{eq} \tag{11}$$

which is used with the relaxation equation of,

$$\begin{aligned} g_i(\mathbf{x} + \mathbf{e_i}\Delta t, t + \Delta t) - g_i(\mathbf{x}, t) = -\tau_g^{-1} \left(g_i(\mathbf{x}, t) - g_i^{eq} \right) \\ + \left(1 - (2\tau_g)^{-1}\right) \delta t q_i + \left(\tau_g^{-1} - \tau_f^{-1} \right) Z_i \Phi_i. \end{aligned} \tag{12}$$

Here $Z_i = \mathbf{e_i} \cdot \mathbf{u} - 0.5\,(\mathbf{u} \cdot \mathbf{u})$, $\Phi_i = f_i - f_i^{eq}$ and $q_i = \omega_i \rho E / c_s^2$. Here, the spatial and temporal states on the populations have been temporarily reinstated to indicated the evolution of these values. All other variable quantities are taken at '$(\mathbf{x}, t)$'. Similar to viscosity and τ_f, the relaxation time τ_g is related to the thermal diffusivity of the fluid $\alpha = \frac{k}{\rho C_p} = (\tau_g - 0.5)\,(\Delta x^2)/(3\Delta t)$.

The full total energy approach presented in [8] allows for a detailed series of forcing terms that control the collision and relaxation of the respective populations that were not required for this study.

2.2. DEM - Solids and coupling

The discrete element method treats the solid component of suspensions as a collection of independent point particles with individual geometric and material properties. The forces acting on these are summed and integrated according to Newton's second law to determine the kinematic motion of each particle. Forces acting on the particles in this study arise from hydrodynamic interactions with the suspending fluid and contact with other particles or walls. In a more general setting, gravity and electro-static or -magnetic forces could contribute to the motion of particles.

The calculation of the hydrodynamic forces acting on a particle form the fundamental basis to the numerical coupling of the solid and fluid models. This work utilises the strategy presented by Noble and Torczynski [27] to modify the relaxation of the fluid LBM population to account for the presence of the solid particles. This sees Equation 5 become,

$$f_i(\mathbf{x}+\mathbf{e_i}\Delta t, t+\Delta t) - f_i(\mathbf{x},t) = -\tau_f^{-1}\left[1-B\right]\left(f_i(\mathbf{x},t) - f_i^{eq}(\mathbf{x},t)\right) + B\Omega_i^s. \quad (13)$$

Here B represents the fraction of the unit cell surrounding an LBM node that is covered by a solid particle, shown in Figure 1. Ω_i^s represents a collision function for interactions between the LBM population and the solid particles. In this study, Noble and Torczynksi's [27] non-equilibrium bounceback approach is used,

$$\Omega_i^s = f_{-i}(\mathbf{x},t) - f_i(\mathbf{x},t) + {f_i}^{eq}(\rho,\mathbf{u}_p) - {f_{-i}}^{eq}(\rho,\mathbf{u}), \quad (14)$$

which utilises the particle velocity, $\mathbf{u}_p$. Here $-i$ indicates the velocity direction pointing in the opposite direction to i.

The hydrodynamic force and torque acting on a particle centred at $\mathbf{x}_p$ can be, respectively, found by [28],

$$\mathbf{F}_f = \frac{\Delta x^2}{\Delta t}\sum_r B_r\left(\sum_i \Omega_i^s \mathbf{e_i}\right), \quad (15)$$

and,

$$\mathbf{T}_f = \frac{\Delta x^2}{\Delta t} \sum_r (\mathbf{x} - \mathbf{x}_p) \times B_r \left(\sum_i \Omega_i^s \mathbf{e_i} \right). \tag{16}$$

In these expressions, r counts the nodes that map a particle to the lattice.

2.3. Conjugate heat transfer for the total energy LBM

As noted previously, temperature must be continuous across the boundary in order to ensure CHT conditions at the interface of disparate media. The methods discussed in [22, 23] are suitable for the passive scalar LBM where temperature is the conserved quantity. These methods are not applicable to the total energy LBM required to model temperature-dependent viscosity fluids. This is because, in this study, total energy is the conserved quantity (i.e. zeroth moment) of the thermal population. To illustrate why a CHT approach that conserves the zeroth moment is not useful, consider a stationary case where C_p, the local specific heat, varies between two adjacent nodes such as for a boundary between two media. The total energy model being used here, proposed by Guo et al.[8], conserves the quantity $\rho E = \rho(C_p T + 0.5\mathbf{u}^2)$. As the quantity ρE will be continuous between these two locations, there will be a step change in temperature that is proportional to the ratio of C_p values. To meet CHT requirements, this behaviour must be reversed such that temperature is continuous and there is a step change in total energy. Pareschi et al.[18] developed a CHT scheme for a total energy conserving form of the entropic LBM. In this section, this methodology has been adapted to the LBM construction used in this work.

The approach of Pareschi et al.[18] is a strictly off-grid method. This is in the sense that the true interface of the two media is located between nodes. In the current implementation, the boundary is assumed to lie at the mid-point of these locations. The rationale of this method is that the interface between the two components is treated as a boundary between the respective regions. The CHT conditions are enforced by modification of the populations that are streamed across the boundary.

The first step in the procedure is to identify the temperature of the interface based on the CHT conditions. Given the interface is located off-grid, this computation will necessarily occur between the current node and its nearest neighbour with the adjacent media. This is then used to estimate the temperature at the local node by interpolating between the interface temperature and that at the node in the opposite direction to the interface. This is illustrated for a straight boundary in Figure 2.

These values are then used to determine the local temperature gradients in the appropriate Cartesian directions of the lattice. Calculating these gradients is a non-local process which degrades the computational performance of this model. This occurs due to the need to access data from neighbouring LBM nodes. The time taken for this to occur depends on the computational architecture used for simulation but may require communication between physically separate compute cores. The key step in this CHT implementation is the use of these temperature gradients to determine a correction term for the equilibrium expression of populations streaming across the boundary. This has the effect of modifying the populations such that they are streamed from a location with the computed interface temperature. The correction terms,

$$h_i^{eq,*} = \frac{w_i}{c_s^2}\left(c_s^2\tau_g\rho c_v K_\gamma \partial_\gamma T + 2u_\delta P_{\gamma\delta}\right) + \frac{w_i}{c_s^4}\left(c_s^2\tau_g\rho c_v\left(u_\gamma K_\delta \partial_\delta T + u_\delta K_\gamma \partial_\gamma T\right) + \left(2c_s^2 + 0.5\rho c_v T\right)P_{\gamma\delta}\right) \quad (17)$$

are added to the equilibrium values of the total energy energy population prior to the collision step occurring. Here γ and δ refer to the Cartesian directions of the lattice in Einstein notation and $P_{\gamma\delta} = \sum_i c_{i\gamma}c_{i\delta}\left(f_i - f_i^{eq}\right)$. The K values are a conductivity correction term to be applied to the temperature gradient. This term takes a value of 1 if the conductivity decreases between nodes in the indicated direction, -1 if conductivity increases or 0 if there is no change. Note that this overall correction is of a slightly different form to that presented by Pareschi et al.[18]. This is due to the zeroth moment of the energy population

calculating $2\rho E$ in [18] compared to ρE in the model of Guo et al.[8] used in this work. An advantage of this strategy is that the form of the correction term is general for both two- and three-dimensional problems.

2.4. Verification and validation

2.4.1. Relative viscosity of particle suspensions

To validate the model for suspension flow, the effective viscosity for a variety of solid volume fraction (ϕ) cases was calculated and compared to previous results from the literature. In a general setting of spheres immersed within a Newtonian fluid, the presence of the solids causes the apparent viscosity of the suspension to increase. This is noted to occur rapidly as ϕ of the suspension approaches the maximum packing (for particles of the same size) of approximately 64% [29]. To test this, a numerical rheometer was designed such that a single layer of particles was located in the centre of the domain. These were set to half the radius of the free particles to allow better packing and a smoother platen surface. A constant force, $F_{applied}$, was applied to this platen to shear the fluid. The measured steady-state velocity of the platen indicated the velocity gradient, $\partial U/\partial y$, to the walls parallel to platen. This allowed the effective viscosity, μ_E, of the suspension to be measured using,

$$\tau = \frac{F_{applied}}{A} = \mu_E \frac{\partial U}{\partial y}, \tag{18}$$

with τ being the shear stress in the fluid over plan area A. The addition of particles to either one or both sides of the shearing platen alters the ϕ of the suspension being tested. The relative viscosity, μ_R, of the suspension is the ratio of μ_E to the viscosity of the base fluid. A schematic layout of this test domain is illustrated in Figure 3. The physical grid spacing ($\Delta x = 1.5625\times\ 10^{-5} m$), time step ($\Delta t = 4\mu s$), and relaxation time ($\tau_f = 1.0$) result in a fluid viscosity of approximately $\nu = 1.02 \times 10^{-5} m^2/s$. The domain height was set to $H = 0.002m$ and the shearing force on the platen was set at 4 μN. Tests were run until a steady platen velocity was reached.

Due to fluid-particle and particle-wall interactions, the effective viscosity of the fluid increases with ϕ. A number of empirical correlations for this behaviour can be found in the literature [1–5]. What can be noted from these correlations is that the behaviour of the suspension becomes more sensitive to experimental layout and material properties as the particle fraction increases. This is evidenced by the increasing spread of values for the correlations presented in Figure 4. In this study, the 'Model 1' results calculate the relative viscosity by comparison to the input fluid viscosity. 'Model 2' compares the suspension viscosity against the viscosity of the fluid as calculated by repeating the test with no free particles present. These results are compared against a number of experimentally validated correlations for the relative viscosity of suspensions from the literature (Equations 1- 4).

In Figure 4, the rheometer has particles on both sides of the shearing platen in order to provide a symmetrical model of the Couette-type rheometer that is used in many experimental studies. Here the numerical results best fit the predictions of the Eilers [3, 4] and Mooney [1] correlations. The discrepancy between the numerical model and the correlations is however similar to that seen elsewhere in the literature e.g. [6]. It should also be noted that the correlations and numerical results presented by Thorimbert et al.[6] are developed using a smooth shearing platen. It is unsurprising that with the rougher platen used in this model that the suspension appears more viscous as both fluid and particle interactions with the platen are increased. The two sets of results in this figure further illustrate the difference in behaviour that the choice of platen can make. In Figure 4a, a densely packed platen has been used to more closely imitate a smooth surface shearing the fluid. This layout will more strongly interact with the free particles, but it will also experience greater viscous drag from the free fluid. In Figure 4b, the platen is much more sparsely packed - the fraction of the shearing plane covered by particles is reduced by a factor of approximately nine. This reduces both the amount of particle interaction with the platen and the effective drag upon it. As the thickness of the effective shearing platen is the same through the height of the domain, these two layouts yield effectively

similar velocity profiles through the sheared fluid. It can be seen that the sparser platen does serve to better match the correlation predictions, particularly at ϕ below about 0.3.

Figure 5 presents the relative viscosity results for a rheometer with particles situated on both sides of a sparsely packed platen. Here the 'T' results represent simulations performed with a temperature thinning fluid,

$$\nu = \nu_0 e^{-T}, \tag{19}$$

at a constant dimensionless temperature of $T = 1$, ν_0 represents the unmodified fluid viscosity. As an incompressible fluid is being studied the conversion between dynamic and kinematic viscosities is valid. In the thinner fluid, the relative viscosity of the suspension is significantly increased over the isothermal case. This behaviour was observed experimentally by Konijn et al.[30] and highlights that the relative viscosity of a fluid may not solely be dependent on ϕ. Of the potential explanations for this presented by Konijn et al., grain-inertia effects are possibly the most likely explanation in the current setting. As particles can move more freely in the thinner fluid, more of the input shearing force is required to overcome particle momentum when they collide with the shearing platen. This results in a greater apparent viscosity of the suspension, especially with increasing ϕ.

In all cases presented here, it is important to observe that the fundamental physics of suspensions is being captured accurately by the model.

2.4.2. Transient conjugate heat transfer modelling

To quantify the performance of this implementation, three test cases were performed. The first was a two-medium bar, the second a case of flow parallel to an interface bounded by sinusoidal temperature boundaries, and the final a case of radial heat transfer.

Firstly, an end-heated 1D bar was used as an initial test case to demonstrate the performance of the CHT method. In this investigation for a bar of length $L = 59\Delta x$, the left ($0 \leq x \leq L/2$) and right ($L/2 \leq x \leq L$) half domain values

were 1/6 and 1/2 for conductivity, k, and 1 and 2 for heat capacity. Constant temperature boundaries of T=1 and 0 were held at the boundaries x=0 and x=1, respectively. Note that these are in lattice units. Consequently, $\Delta t = 1$ is used for this test as well as for the subsequent examples. The steady-state result for this situation can be determined from the CHT relations and the knowledge that linear temperature profiles will be created between the boundaries and the media interface. The interface temperature for this case is,

$$T_{Interface} = \frac{k_1 T_H + k_2 T_L}{k_1 + k_2}. \tag{20}$$

In Figure 6 it can be seen that the total energy LBM model is able to capture this behaviour accurately. The effect of the CHT correction creating a continuous temperature profile and step change in total energy at the interface can also been seen in this diagram. The transient performance of the LBM model was also examined by comparing the temperature development at $x = L/4, L/2$ and $3L/4$ to the analytic model developed in the work of Sun and Wichman [22, 23, 31]. As can be seen in Figures 6 and 7, this behaviour is also captured accurately. In particular, the model approaches the exact solution at the interface. The convergence of the model to steady-state can also be seen after approximately 7,500 steps.

The case of flow parallel to an interface has previously been used [15, 21] as an example of steady-state heat flow under complex boundary conditions. The domain used (Figure 8) is rectangular with length L and height H with $(x, y) \in ([0, L] \times [0, H])$. This is split at the point $y = H/2$ into two regions of differing material properties. The upper and lower boundaries of the full domain are held at a constant temperature profile described by $T(x, 0) = T(x, H) = cos(2\pi x/L)$. A constant horizontal velocity, U, flows through the entire domain in a periodic manner. The analytical solution for this problem at steady-state is given in Li et al.[21], although it should be noted that the term $(a_1^2 - 1)$ in the numerator of Equation 37 of this paper should read $(a_1^2 - 1)a_3$ [1]. Dimensionless

[1] This was confirmed via direct correspondence with the leading author, Like Li (31 January

quantities were used to test the model within a domain of $(H \times L) = (64 \times 64)$. The upper and lower half domain values were 1/6 and 1 for conductivity, and 1/2 and 2 for heat capacity. Density, ρ, was held at unity throughout the entire test section. As per Li et al.[21], the velocity was chosen such that a Peclet number of $Pe = \frac{UHC_{p,lower}}{k_{lower}} = 20$ was enforced. LBM temperature profiles at $x/L = 0.0625, 0.25, 0.5$ and 0.75 have been generated and compared to the analytical solution at these locations. These are presented in Figure 9. As can be seen, the LBM results are able to very closely capture the analytic results.

To demonstrate the model's ability to resolve CHT on curved boundaries, the radial test case presented in Li et al.[21] and Karani and Huber [15] has been analysed. This test case has a radial layout, as shown in Figure 10. Here the temperature of the outer boundary of the outer layer varies with radial position as $T(R_2, \theta) = cos(2\theta)$. The steady-state analytic solution for this problem is provided in Li et al.[21]. It should also be noted that this test case was presented in Pareschi et al.[18] but with a slightly different fixed temperature boundary condition. This scenario was simulated until a steady-state was reached for four levels of grid resolution (between 16 and 128 lattice cells across the radius of the domain). In this model, the outer annulus was prescribed material properties of $k = 100/6$ and C_p of 10, while the inner region was prescribed $k = 1/6$ and C_p of 1 (lattice units). An example of the temperature contours generated by the model at steady-state can be seen in Figure 11. It should be noted here that the small circular contours around the edge of the interface of the two media can be viewed as artefacts associated with converting a circular boundary to a Cartesian lattice grid. In particular, this is believed to be associated with correctly identifying the missing populations at those locations. Also, these locations are where the assumption that the interface is midway between the nodes is most incorrect. The L_2 norm of these different grid resolutions was plotted against the radial resolutions to estimate the convergence properties of the implementation. The result of this is given in Figure 12. The order of

2018).

convergence was noted to be 0.52, which is less than the results given by Pareschi et al.[18]. The difference in L_2 error magnitude between that and this work can be attributed to the different temperature measurements used to compile the L_2 figure. In Figure 12, the LBM profile was compared against the analytic solution along the radius of the full domain at $\theta = 0$. In Pareschi et al.[18], the temperature along the interface of the two regions was used to assess the model.

The total energy approach for CHT presented above supposed that the interface between two media was stationary. To model transient suspensions, the method needs to be adapted to accommodate changing interface positions. This was achieved by labelling the component of a given node based on its solid coverage at a given point in time. By comparing the value of this flag with that of its neighbours, the presence and orientation of component boundaries relative to the node can be identified. Once the directional orientation is known in terms of the closest lattice velocity direction, the interface is assumed to lie halfway between the current node and the neighbouring node in that direction. From this point, the presented CHT algorithm can be applied.

To illustrate the calculation of the normal direction, a 2D example is given for simplicity (see Figure 13). Here, positive flag values are assigned to the solid (S) and fluid (F) nodes. The normal located at node e can then be calculated with,

$$\hat{\mathbf{n}} = \frac{\mathbf{n}}{|\mathbf{n}|}, \tag{21}$$

where,

$$\mathbf{n} = \left((c + f + i) - (a + d + f)\,, (a + b + c) - (g + h + i)\right). \tag{22}$$

To ensure consistency in computations for the orientation of the normal, the sign of the vector is swapped if the sum of the surrounding nodes is less than the same number (eight in 2D) of the central node (here e). When the flag value of S is greater than F, this ensures that the normal is pointing towards the fluid. The lattice direction, i, closest to the normal can then be found by determining $max(\hat{\mathbf{n}} \cdot \mathbf{c}_i)$.

As a demonstration of CHT being observed, consider a particle moving through a channel of fluid that possesses differing conductivity and heat capacity. Here $k_{solid} = \frac{1}{2}$ and $C_{p,solid} = 3.0$ (lattice units), the respective fluid values are taken as one-third of these. A temperature gradient is applied across the channel with the entire domain intialised at the temperature of the hot wall. As the particle moves it will be cooled by the temperature gradient at a different rate to the surrounding fluid. The particle will represent a disturbance in the temperature field, however the CHT restrictions mean that this will be continuous with fluid's temperature field. This has been applied to a layout similar to the hydrodynamic test case described in Figure 14. In Figures 15 and 16 the desired behaviours for temperature (continuous at particle boundaries) and total energy (step change at particle boundaries and $\frac{C_{p,solid}}{C_{p,fluid}} = 3$ times greater than temperature) can be observed.

3. Numerical investigation of 3D suspension flows

With the model validated, the behaviour of a sheared suspension under a variety of conditions was examined. Numerical rheometry allows a range of configurations and behaviours to be tested efficiently under repeatable conditions. These focused on different combinations of volume fraction, temperature gradient, fluid model and material properties. These demonstrate not only the behaviour of suspensions in an isothermal setting but also when the impacts of temperature-dependent viscosity and conjugate heat transfer were taken into account.

The rheometer model constructed to perform these tests consisted of a layer of regularly packed spheres at its upper and lower surface in the y-direction (see Figure 17). These are translated in opposite directions at a constant velocity to both shear the flow and to provide a boundary to the internal particles. The boundaries in the x- and z-directions are periodic for fluid flow, thermal effects and particle motion. The domain measures $0.002m$ in the x-direction and $0.001m$ in the z-direction. The centres of the spheres in the shearing platens are

separated by $0.0018m$. The particles in these models are all of radius $100\mu m$ and resolved by 6.4 lattice spacings. A time step of $4\mu s$ implies that the kinematic viscosity of the base fluid is approximately $\nu = 1.02 \times 10^{-5} m^2/s$ when the numerical viscosity of the total energy LBM is 1/6. The magnitude of shearing velocity of the two platens was set at $0.1m/s$, corresponding to a shear rate of $\dot{\gamma} = 111.11\ s^{-1}$. Five cases of particle volume fraction were examined, as summarised in Table 1. Note that in the base case, the 120 particles represents those in the two shearing platens. ϕ has been calculated based on the freely moving internal particles only. All cases were run for 80,000 steps. These simulations were run on the Goliath cluster at The University of Queensland and took advantage of the GPUs available on this machine. Simulations took between approximately 20 and 90 minutes to complete depending on the available hardware.

To examine thermal behaviour, the combination of dimensionless temperature gradients used are outlined in Table 2. These can be interpreted as $T_H^{physical}$ = 350K and $T_C^{physical}$ = 300K. It is noted here that for the layout of the rheometer used, the two non-isothermal cases are identical but subject to inverted initial particle positions. The results from these cases should then be approximately symmetric. When a temperature gradient is being applied, the viscosity reduces with temperature according to $\nu = \nu_0 e^{-\beta T}$. Here ν_0 is the viscosity at the cold wall (set numerically as 1/6) and $\beta = 1$.

To demonstrate the influence of conjugate heat transfer on the behaviour of the suspension, the material properties of the solid component were modified in two ways as indicated in Table 3. These changes in material properties conserved the thermal diffusivity of the solid in all cases. The base fluid properties remained unmodified at non-CHT values. In these cases the solids and internal fluid were initialised at the same temperature as the hot wall.

3.1. Numerical rheometry results: non-CHT

To begin, the analysis of suspensions without CHT effects was performed. In practice, this means that the solid and fluid components have the same thermal

properties. To establish a base from which the effects of temperature change and subsequently CHT can be quantified, baseline results for suspension behaviour were established. As presented in Figure 18, these illustrate the average velocity profiles recorded in the central plane of the domain in two ways. Firstly the profiles seen at all ϕ cases without the effects of temperature-dependent viscosity (i.e. the isothermal case); and secondly the base temperature-dependent viscosity fluid profiles when no particles are present. In particular, it can be noted in Figure 18a that as ϕ increases, the presence of particles causes a non-linear perturbation of the velocity profile. The particles cause a reduction in flow velocity through the centre of the channel and steeper flow gradients adjacent to the shearing platens. In Figure 18b, the recorded velocity profiles for a temperature-dependent fluid are consistent in nature with those observed and discussed in previous works [11, 32].

The first comparison that can be made is how the velocity profiles change when a temperature gradient is applied. These are provided in Figure 19. The most noticeable feature of these results is the deviation of the line of stationary flow away from the centre of the channel, consistent with the baseline results. This is particularly noticeable for $\phi5$ and $\phi16$. For both temperature gradient cases, the section of flow adjacent to the heated boundary is very similar for all ϕ cases. This section of flow corresponds to the lowest viscosity region of the domain where the particles provide less of a disturbance to the flow imposed by the shearing platen. Adjacent to the cold boundary, the particle effects dominate for the higher ϕ cases and the fluid effects at lower ϕ. This is indicated by the $\phi28$ and $\phi37$ profiles remaining similar to those seen in the isothermal case whilst $\phi5$ and, to a lesser extent, $\phi16$ more closely resemble the base fluid profile in this region. This behaviour is further highlighted in Figure 20 where the variation of the flow profiles at each non-zero ϕ case are presented. It can be observed here that as ϕ increases, the temperature-dependent behaviour of the fluid reduces and the velocity profile becomes more closely aligned with the base isothermal profile. A characteristic change in the flow profile can be noted to occur between $\phi16$ and $\phi28$ ($\phi \approx 20\%$). Around this point, the 'S'-shape of

the isothermal profile becomes more pronounced compared to the monotonically varying gradient observed with the base temperature-dependent fluid. Figure 21 demonstrates that the presence of particles in the non-CHT case has only a minor impact on the temperature distribution within the fluid. Here the temperature profile becomes slightly non-linear and the temperature throughout the profile is increased. As, thermally speaking, there is no interaction between the solid and fluid in this test case, this variation must be associated with the changing hydrodynamics within the domain. In particular, it is believed that this is caused by viscous heating of the fluid by the freely moving particles. This is discussed further when considering the CHT results. Finally, it was also noted that the vertical migration of particles within the rheometer was negligible for each ϕ case

3.2. Numerical rheometry results: CHT

The material parameters of the solid component were altered in two different ways in order to introduce CHT to the flow. In both cases the 'T' temperature case was simulated. In these cases the thermal relaxation constant, $\omega_g = \tau_g^{-1} = \left(\frac{3k}{\rho C_p} + 0.5\right)^{-1} = 1.0$, was held constant between the solid and fluid components. In Figure 22, the increased properties from Table 3 were implemented, while in Figure 23 the decreased values were used. These investigations were performed to demonstrate CHT effects on the velocity and temperature profiles generated within the sheared rheometer model. Note that in these figures, the 'ϕ0-T' case results have also been added for comparison even though CHT plays no part in this model.

Initially, it can be noted that the velocity profile of the flow remains fundamentally unaltered in the characteristic nature of each ϕ result. The CHT test case with properties increased (Figure 22a) is virtually unchanged from the non-CHT scenario. However, compared to Figure 19a, in Figure 23a there is slightly greater uniformity in the flow of the various ϕ cases in the upper half of the domain. Except for the ϕ37 case, the CHT introduction has caused the average velocity profile to more closely represent the base case. These variations

do not make any qualitative change to the overall behavioural description of the system. As could be expected, there is however a much more noticeable change in average temperature profiles when CHT is introduced to the flow. In both the CHT and non-CHT models the small measure of the variation in temperature profiles between ϕ cases may be attributed to viscous heating resulting from the increase in viscosity associated with particles in suspension. The Brinkman number for a Couette flow is defined as,

$$Br = \frac{\mu_0 U_{max}^2}{k(T_H - T_C)}, \tag{23}$$

and corresponds to the ratio of viscous and conductive heat transfer effects. An increase in Br, such as through the increase in viscosity, corresponds to increased viscous heating. In both CHT cases, the temperature profiles are more widely distributed than in the non-CHT case (Figure 21a). The variations observed in Figure 22b occur mostly in the centre of the domain and are most significant for the $\phi 28$ and $\phi 37$ cases. Here, the variation is more likely to be associated with the increased heat capacity of the particles compared to the surrounding fluid. This corresponds to a region of comparatively low speed flow, better allowing heat to accumulate in this region especially as the fraction of particles increases. In Figure 23b, the wider spread of temperature variation occurs for all ϕ cases and is more noticeable in the upper half of the domain. This can be attributed to corresponding reduction in the k value for the suspension due growing proportion of solids in suspension. This serves to again slightly increase the Br of the flow and the corresponding viscous heating effect.

4. Summary

In this paper, a methodology for studying particle suspensions exposed to thermal effects was presented and used to study the behaviour of sheared systems. This methodology comprised a coupled approach of a total energy conserving lattice Boltzmann method and the discrete element method. These, in combination with an appropriate interface boundary condition, allowed the

model to resolve phenomena associated with temperature-dependent viscosity and conjugate heat transfer.

This model was validated through the calculation of the relative viscosity of suspended spheres at a range of solid volume fractions. The numerical results presented here firstly demonstrated the sensitivity of the measurement of this parameter to the layout of the rheometer. However, the model was able to reproduce the fundamental physics of suspension behaviour at low and medium ϕ. The model also highlighted the apparent dependency of relative viscosity on the temperature of the suspension. This corroborates results seen by physical experiments in the literature.

Finally, the model was used to interrogate the macroscopic properties of sheared suspensions when temperature-dependent viscosity and conjugate heat transfer are present. This highlighted how the behaviour of temperature-dependent viscosity is gradually dominated by particle derived behaviours as the solid volume fraction increases. In the tests performed, the presence of conjugate heat transfer was not observed to strongly influence the velocity profile of a sheared suspension but did contribute to a small amount of shear heating to the temperature profiles.

The results presented in this work indicate two avenues for future work. The first would be to conduct a parametric study of sheared suspensions to propose a new relative viscosity model that takes into account the presence of a temperature-dependent viscosity fluid. The second would be to conduct a more detailed examination of how particle properties could be augmented to exacerbate and control the behaviours observed in this study. Achieving this more subtle control of the temperature and velocity behaviour could allow for optimization of industrial processes where transport of particle suspensions plays a fundamental role. For example, the changing velocity profiles in the suspension could be utilised to assist in separating contaminants from a flow or guiding more suspended particles to a target location within a structure. Such industrial examples could include chemical manufacture, material processing and separation, or transport such as in hydraulic fracturing.

Acknowledgements

Support of this work through the Australian Government Research Training Program Scholarship, the UQ School of Mechanical and Mining Engineering and the Australian Petroleum Production and Exploration Association (K.A. Richards Scholarship) is gratefully acknowledged by the authors. D. Weatherley is acknowledged for the assistance in the development of the coupled LBM-DEM model.

References

References

[1] R. Pal, Rheology of suspensions of solid particles in power-law fluids, The Canadian Journal of Chemical Engineering 93 (1) (2015) 166–173. doi:10.1002/cjce.22114.
URL http://dx.doi.org/10.1002/cjce.22114

[2] J. F. Morris, F. Boulay, Curvilinear flows of noncolloidal suspensions: The role of normal stresses, Journal of Rheology 43 (5) (1999) 1213–1237. arXiv:https://doi.org/10.1122/1.551021, doi:10.1122/1.551021.
URL https://doi.org/10.1122/1.551021

[3] J. R. Clausen, D. A. Reasor, C. K. Aidun, The rheology and microstructure of concentrated non-colloidal suspensions of deformable capsules, Journal of Fluid Mechanics 685 (2011) 202–234. doi:10.1017/jfm.2011.307.
URL http://journals.cambridge.org.ezproxy.library.uq.edu.au/article_S0022112011003077

[4] I. E. Zarraga, D. A. Hill, D. T. Leighton, The characterization of the total stress of concentrated suspensions of noncolloidal spheres in Newtonian fluids, Journal of Rheology 44 (2) (2000) 185–220. arXiv:https://doi.org/10.1122/1.551083, doi:10.1122/1.551083.
URL https://doi.org/10.1122/1.551083

[5] B. Lecampion, D. I. Garagash, Confined flow of suspensions modelled by a frictional rheology, Journal of Fluid Mechanics 759 (2014) 197–235. doi:10.1017/jfm.2014.557.

[6] Y. Thorimbert, F. Marson, A. Parmigiani, B. Chopard, J. Latt, Lattice Boltzmann simulation of dense rigid spherical particle suspensions using immersed boundary method, Computers & Fluids 166 (2018) 286 – 294. doi:https://doi.org/10.1016/j.compfluid.2018.02.013.
URL http://www.sciencedirect.com/science/article/pii/S0045793018300690

[7] Z. Guo, T. Zhao, Lattice Boltzmann simulation of natural convection with temperature-dependent viscosity in a porous cavity, Progress in Computational Fluid Dynamics 5 (1/2) (2005).

[8] Z. Guo, C. Zheng, B. Shi, T. S. Zhao, Thermal lattice Boltzmann equation for low Mach number flows: Decoupling model, Physical Review E 75 (2007) 036704. doi:10.1103/PhysRevE.75.036704.
URL http://link.aps.org/doi/10.1103/PhysRevE.75.036704

[9] X.-R. Zhang, Y. Cao, A lattice Boltzmann model for natural convection with a large temperature difference, Progress in Computational Fluid Dynamics, an International Journal 11 (5) (2011) 269–278. arXiv:https://www.inderscienceonline.com/doi/pdf/10.1504/PCFD.2011.042179, doi:10.1504/PCFD.2011.042179.
URL https://www.inderscienceonline.com/doi/abs/10.1504/PCFD.2011.042179

[10] Y. Cao, Variable property-based lattice Boltzmann flux solver for thermal flows in the low Mach number limit, International Journal of Heat and Mass Transfer 103 (2016) 254 – 264. doi:https://doi.org/10.1016/j.ijheatmasstransfer.2016.07.052.
URL http://www.sciencedirect.com/science/article/pii/S0017931016312078

[11] J. McCullough, S. Aminossadati, C. Leonardi, Transport of particles suspended within a temperature-dependent viscosity fluid using coupled lbm–dem, International Journal of Heat and Mass Transfer 149 (2020) 119159. doi:https://doi.org/10.1016/j.ijheatmasstransfer.2019.119159.
URL http://www.sciencedirect.com/science/article/pii/S0017931019342632

[12] A. Eshghinejadfard, D. Thevenin, Numerical simulation of heat transfer in particulate flows using a thermal immersed boundary lattice Boltzmann method, International Journal of Heat and Fluid Flow 60 (2016) 31 – 46. doi:http://dx.doi.org/10.1016/j.ijheatfluidflow.2016.04.002.
URL http://www.sciencedirect.com/science/article/pii/S0142727X16301126

[13] R. H. Khiabani, Y. Joshi, C. K. Aidun, Heat transfer in microchannels with suspended solid particles: Lattice-Boltzmann based computations, Journal of Heat Transfer 132 (4) (2010) 041003–041003. doi:10.1115/1.4000860.
URL http://dx.doi.org/10.1115/1.4000860

[14] Z. Hashemi, O. Abouali, R. Kamali, Thermal three-dimensional lattice Boltzmann simulations of suspended solid particles in microchannels, International Journal of Heat and Mass Transfer 65 (0) (2013) 235 – 243. doi:http://dx.doi.org/10.1016/j.ijheatmasstransfer.2013.06.005.
URL http://www.sciencedirect.com/science/article/pii/S0017931013004705

[15] H. Karani, C. Huber, Lattice Boltzmann formulation for conjugate heat transfer in heterogeneous media, Physical Review E 91 (2015) 023304. doi:10.1103/PhysRevE.91.023304.
URL http://link.aps.org/doi/10.1103/PhysRevE.91.023304

[16] Y. Hu, D. Li, S. Shu, X. Niu, Full Eulerian lattice Boltzmann model for conjugate heat transfer, Physical Review E 92 (2015) 063305. doi:10.

1103/PhysRevE.92.063305.
URL http://link.aps.org/doi/10.1103/PhysRevE.92.063305

[17] A. A. Mohamad, Q. W. Tao, Y. L. He, S. Bawazeer, Treatment of transport at the interface between multilayers via the lattice Boltzmann method, Numerical Heat Transfer, Part B: Fundamentals 67 (2) (2015) 124–134. arXiv:http://dx.doi.org/10.1080/10407790.2014.949563, doi:10.1080/10407790.2014.949563.
URL http://dx.doi.org/10.1080/10407790.2014.949563

[18] G. Pareschi, N. Frapolli, S. S. Chikatamarla, I. V. Karlin, Conjugate heat transfer with the entropic lattice Boltzmann method, Physical Review E 94 (2016) 013305. doi:10.1103/PhysRevE.94.013305.
URL http://link.aps.org/doi/10.1103/PhysRevE.94.013305

[19] K. Guo, L. Li, G. Xiao, N. AuYeung, R. Mei, Lattice Boltzmann method for conjugate heat and mass transfer with interfacial jump conditions, International Journal of Heat and Mass Transfer 88 (0) (2015) 306 – 322. doi:http://dx.doi.org/10.1016/j.ijheatmasstransfer.2015.04.064.
URL http://www.sciencedirect.com/science/article/pii/S0017931015004342

[20] M. Seddiq, M. Maerefat, M. Mirzaei, Modeling of heat transfer at the fluid-solid interface by lattice Boltzmann method, International Journal of Thermal Sciences 75 (2014) 28 – 35. doi:http://dx.doi.org/10.1016/j.ijthermalsci.2013.07.014.
URL http://www.sciencedirect.com/science/article/pii/S1290072913001713

[21] L. Li, C. Chen, R. Mei, J. F. Klausner, Conjugate heat and mass transfer in the lattice Boltzmann equation method, Physical Review E 89 (2014) 043308. doi:10.1103/PhysRevE.89.043308.
URL http://link.aps.org/doi/10.1103/PhysRevE.89.043308

[22] J. McCullough, C. Leonardi, B. Jones, S. Aminossadati, J. Williams, Lattice Boltzmann methods for the simulation of heat transfer in particle suspensions, International Journal of Heat and Fluid Flow 62, Part B (2016) 150 – 165. doi:http://dx.doi.org/10.1016/j.ijheatfluidflow.2016.11.005.
URL http://www.sciencedirect.com/science/article/pii/S0142727X16303691

[23] J. McCullough, C. Leonardi, B. Jones, S. Aminossadati, J. Williams, Investigation of local and non-local lattice boltzmann models for transient heat transfer between non-stationary, disparate media, Computers & Mathematics with Applications (2018). doi:https://doi.org/10.1016/j.camwa.2018.01.018.
URL http://www.sciencedirect.com/science/article/pii/S0898122118300348

[24] Z. Hashemi, O. Abouali, R. Kamali, Three dimensional thermal lattice Boltzmann simulation of heating/cooling spheres falling in a Newtonian liquid, International Journal of Thermal Sciences 82 (0) (2014) 23 – 33. doi:http://dx.doi.org/10.1016/j.ijthermalsci.2014.03.008.
URL http://www.sciencedirect.com/science/article/pii/S1290072914000696

[25] TCLB Reference Manual (2019).
URL https://docs.tclb.io/

[26] ESyS-Particle Community Wiki (2019).
URL http://www.esys-particle.org/wiki/

[27] D. R. Noble, J. R. Torczynski, A lattice-Boltzmann method for partially saturated computational cells, International Journal of Modern Physics C 9 (8) (1998) 1189–1201.

[28] B. K. Cook, D. R. Noble, J. R. Williams, A direct simulation method for

particle-fluid systems, Engineering Computations 21 (2/3/4) (2004) 151–168.

[29] J. J. Stickel, R. L. Powell, Fluid mechanics and rheology of dense suspensions, Annual Review of Fluid Mechanics 37 (1) (2005) 129–149. arXiv:http://dx.doi.org/10.1146/annurev.fluid.36.050802.122132, doi:10.1146/annurev.fluid.36.050802.122132.
URL http://dx.doi.org/10.1146/annurev.fluid.36.050802.122132

[30] B. Konijn, O. Sanderink, N. Kruyt, Experimental study of the viscosity of suspensions: Effect of solid fraction, particle size and suspending liquid, Powder Technology 266 (2014) 61 – 69. doi:https://doi.org/10.1016/j.powtec.2014.05.044.
URL http://www.sciencedirect.com/science/article/pii/S0032591014005014

[31] Y. Sun, I. S. Wichman, On transient heat conduction in a one-dimensional composite slab, International Journal of Heat and Mass Transfer 47 (6–7) (2004) 1555 – 1559. doi:http://dx.doi.org/10.1016/j.ijheatmasstransfer.2003.09.011.
URL http://www.sciencedirect.com/science/article/pii/S0017931003005337

[32] T. Myers, J. Charpin, M. Tshehla, The flow of a variable viscosity fluid between parallel plates with shear heating, Applied Mathematical Modelling 30 (9) (2006) 799 – 815. doi:https://doi.org/10.1016/j.apm.2005.05.013.
URL http://www.sciencedirect.com/science/article/pii/S0307904X05001125

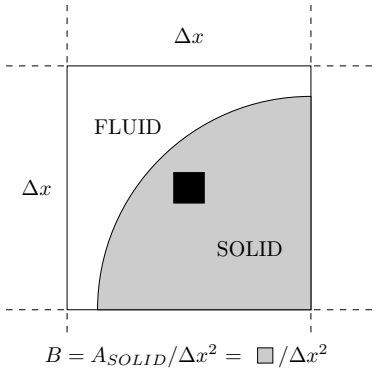

Figure 1: Strategy for calculating the nodal coverage fraction B for use in the PSM method. Interface nodes for particle boundaries are identified as $B \in (0, 1)$. Note that the solid and dotted lines in this figure are offset from the lattice grid linking nodes by $\Delta x/2$.

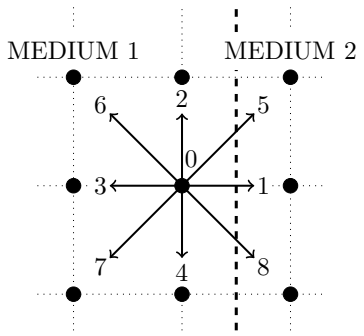

Figure 2: An example of finding temperatures within the total energy CHT model. To find the interface temperature along the dotted line, the CHT equations are solved between the '0' node and that in the '1' direction. The temperature at '0' is then estimated from the interface value and that at the node in the '3' direction.

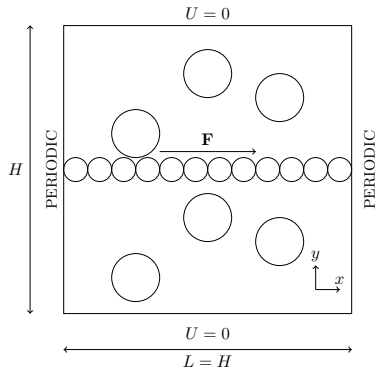

(a) Domain layout

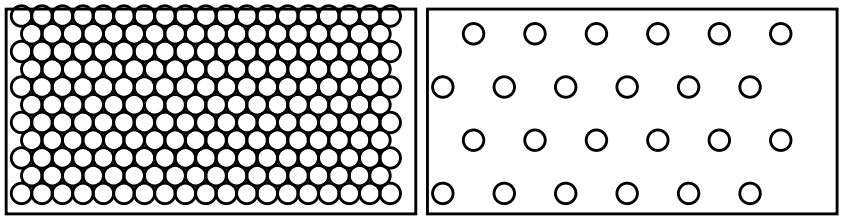

(b) Top view of dense platen

(c) Top view of sparse platen

Figure 3: Mid-plane view of the relative viscosity test used to validate the model's hydrodynamics. The model is periodic in the x- and z-directions and measured $0.5H$ out-of-plane. Fluid velocity was fixed at U=0 on the upper and lower walls. Free moving particles were placed either below or on both sides of the central shearing platen. Bounding walls were placed at the top and bottom of the domain to bound the particles within the system. The central platen had a constant force applied to it to shear the fluid and its steady-state velocity provided a measure of the effective viscosity of the suspension. A sparse (b) and dense (c) platen layout was examined.

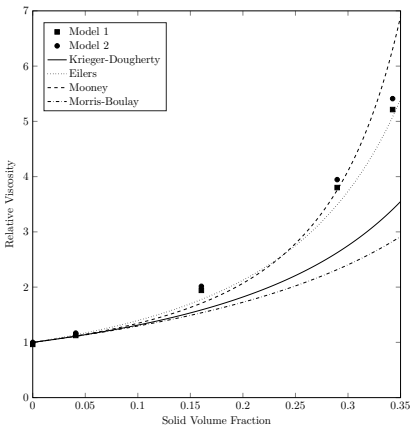

(a) Dense platen

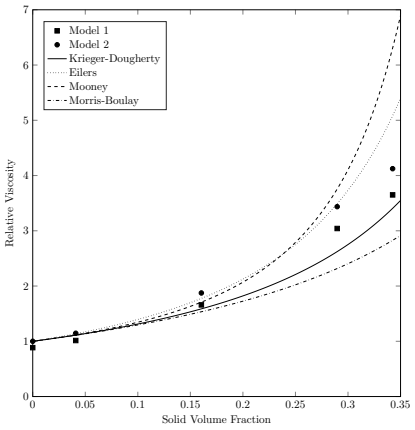

(b) Sparse platen

Figure 4: Relative viscosity results generated by the model with particles located on both sides of the platen. The 'Model 1' results calculate the relative viscosity by comparison to the input fluid viscosity. 'Model 2' compares against the viscosity determined with no free particles present. In (a) the platen is essentially fully covered by non-overlapping particles whereas in (b) the driving platen is sparsely populated with particles. These results indicated the sensitivity of the the relative viscosity to the layout of the rheometer.

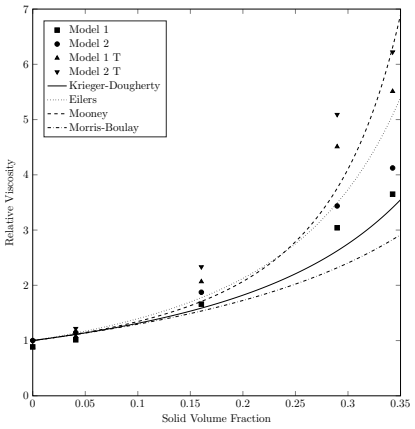

Figure 5: Relative viscosity results with particles on both sides of a sparsely packed platen. The 'T' results indicated simulations run with a temperature-dependent viscosity fluid at T=1 (i.e. $\nu = \nu_0 e^{-1}$).

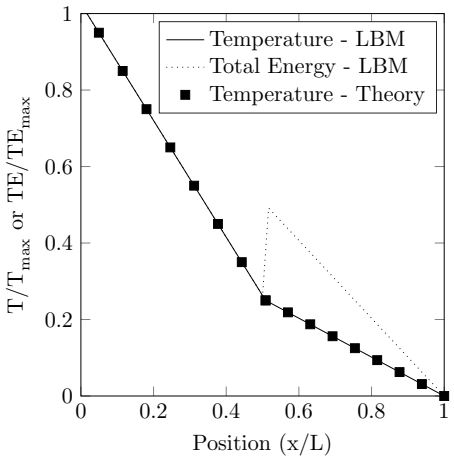

Figure 6: The steady-state bar results for temperature (compared to the analytic result) and total energy. The continuity of temperature and step change in total energy at the interface of the two material regions is clearly visible.

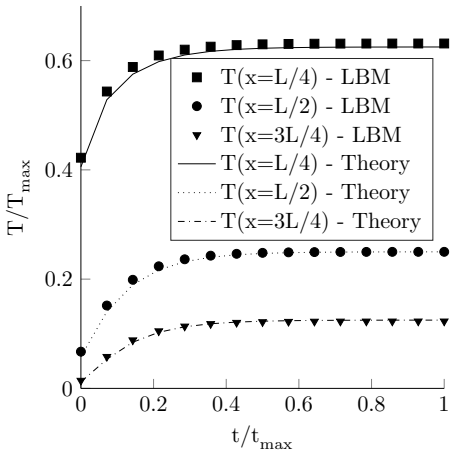

Figure 7: Transient results for temperature at three locations along the two medium bar. The total energy LBM model is able to accurately capture the theoretical behaviour of the Sun and Wichman analytical model [22, 23, 31].

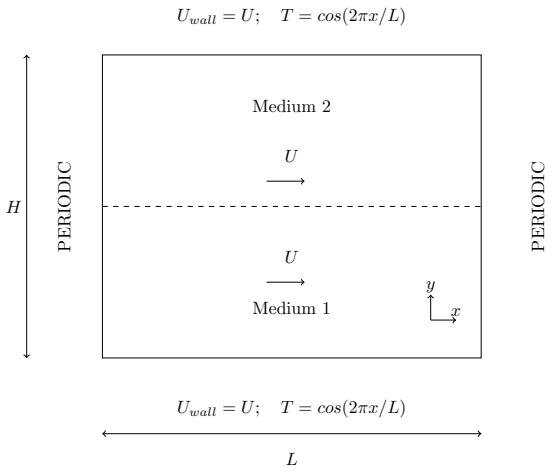

Figure 8: Layout for testing the steady-state LBM and analytic temperature profiles for flow across adjacent media with varying material properties as described in Li et al.[21].

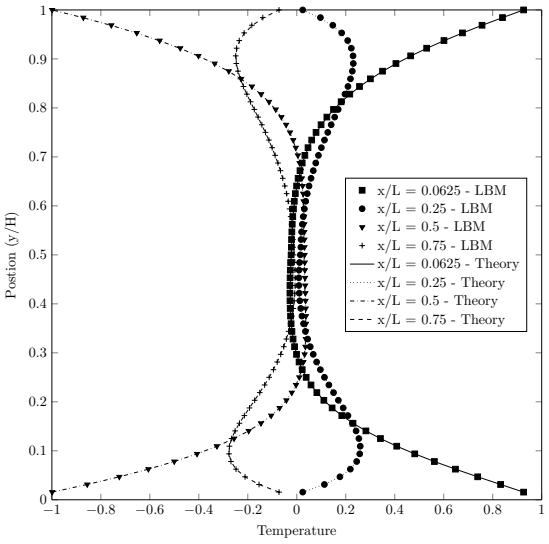

Figure 9: Comparison of steady-state LBM and analytic temperature profiles for flow across adjacent media with varying material properties as described in Li et al.[21]. The difference in profiles is due to the sinusoidal temperature profile along the upper and lower edges of the domain.

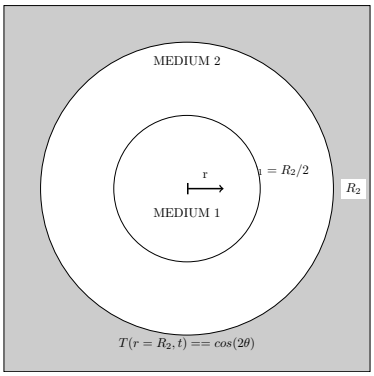

Figure 10: Layout of the two-medium radial test case used to examine the interface model on curved boundaries. Nodes located on the outer boundary of Medium 2 were set to $T(R_2, \theta) = cos(2\theta)$. Those in the grey region beyond were set to the value at R_2 along the same angular line.

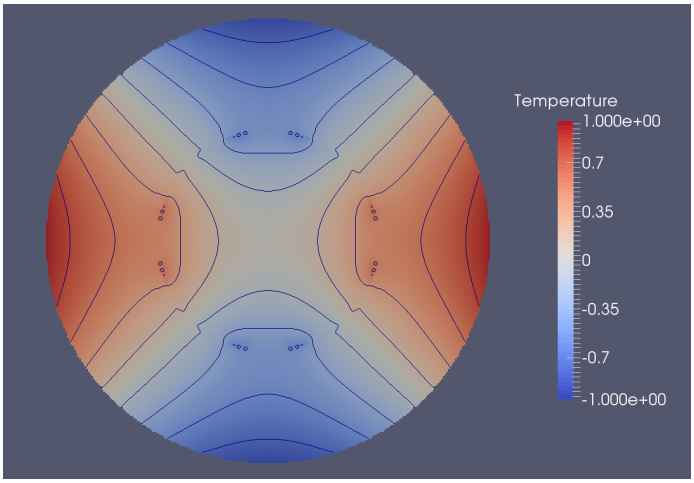

Figure 11: Temperature field and contours for the radial CHT test case. The small, round contour artefacts near the interface of the two media is believed to be associated with identifying the missing populations of the interface and locating a circular boundary onto a Cartesian lattice grid.

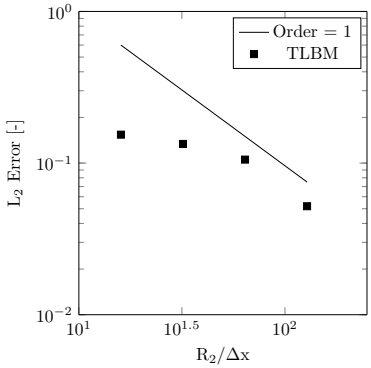

Figure 12: Convergence of the radial LBM results towards the analytic prediction. The order of convergence is estimated at 0.52.

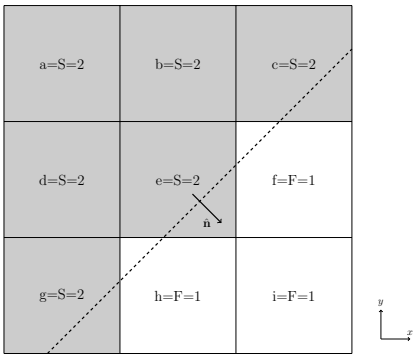

Figure 13: Illustrative 2D schematic for calculating the local direction of the interface (dashed line) normal. Each node is designated as either solid, S, or fluid, F, with a flag value (1 or 2). The flags of the node of interest and its surrounding neighbours are used to determine the direction of the fluid-oriented interface normal, $\hat{\mathbf{n}}$, through use of Equations 21 and 22. This then determines the lattice direction closest to the normal.

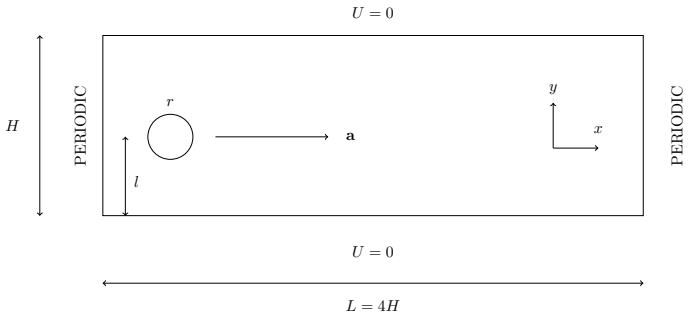

Figure 14: Mid-plane view of terminal velocity test used to verify the model's hydrodynamics. The model is periodic in the out-of-page direction which also had a total depth of $4H$. The particle of radius $r = 0.0001m$ was placed such that $r/l = 0.5$, while $l = H/4$ was used in testing.

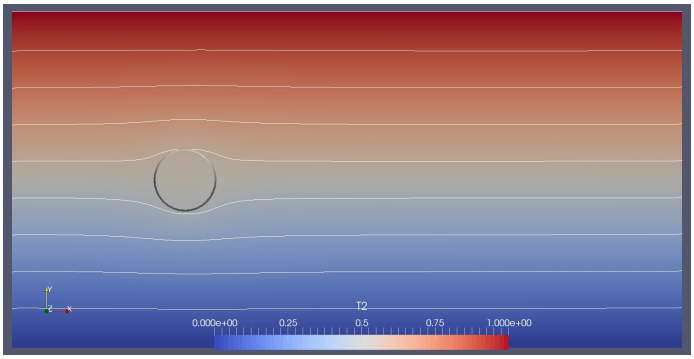

(a) Temperature distribution at $t^* = 0.85$

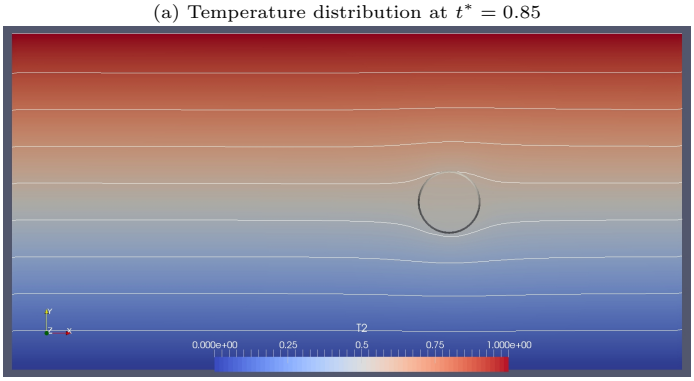

(b) Temperature distribution at $t^* = 1.0$

Figure 15: An example of the temperature distribution around a particle as it moves through a fluid with an applied temperature gradient. The figures are coloured and contoured by dimensionless temperature. Because of the CHT implementation, the temperature field is continuous between media within the total energy conserving LBM model.

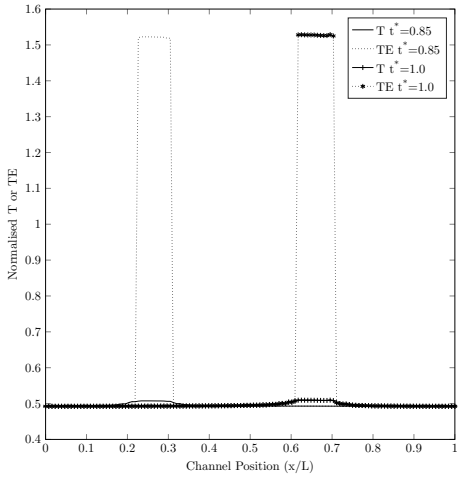

Figure 16: Traces of temperature and total energy along the centre line of the channel at the times presented in Figure 15. The continuity of temperature and step change in total energy are clearly evident.

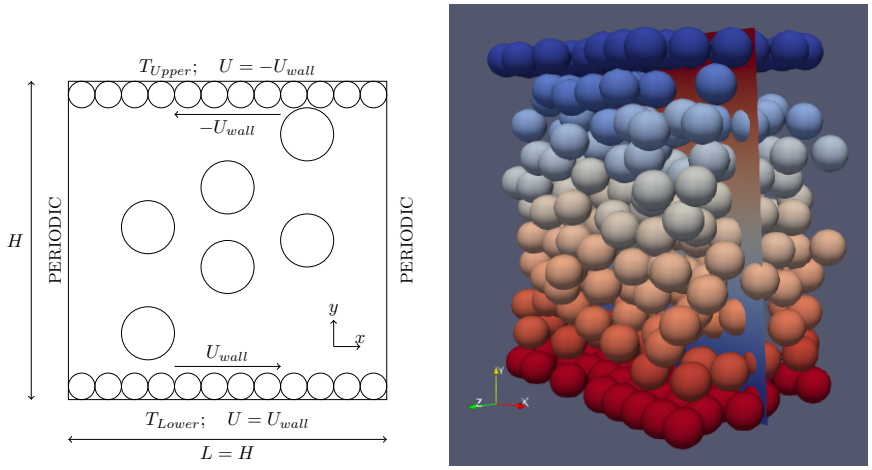

Figure 17: Mid-plane view and 3D illustration of planar shearing test used to explore the macroscopic behaviour of suspensions. The model is periodic in the out-of-page direction which also had a total depth of $0.5H$. Free moving particles were placed between the upper and lower constant velocity shearing platens at various concentrations. The particles in the 3D illustration of $\phi 37$ are coloured by velocity, whilst the plane in the centre indicates the temperature of the fluid.

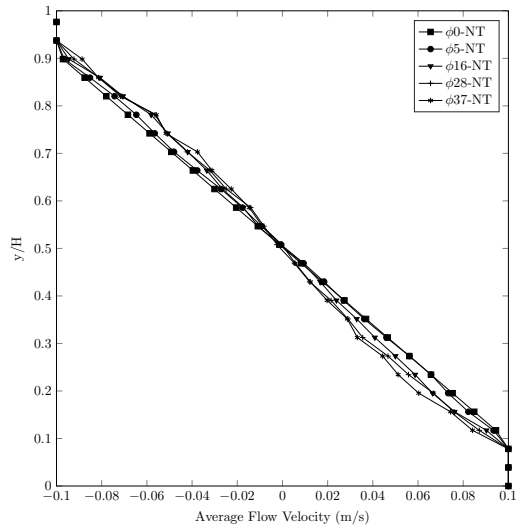

(a) Baseline for non-zero ϕ

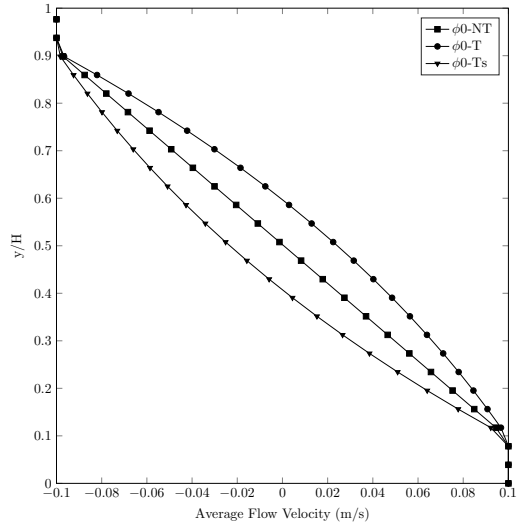

(b) Baseline temperature

Figure 18: Baseline results for the velocity profiles generated within the rheometer. The non-zero ϕ results indicate the profiles generated without temperature-dependent viscosity or CHT effects. The temperature results indicate the profiles generated within the fluid with no particles present under the temperature conditions. The NT results refer to the isothermal model. T and Ts refer to the two temperature cases (see Table 2).

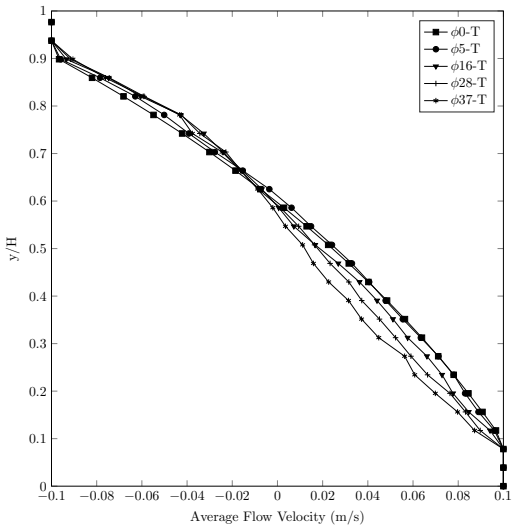

(a) Case 'T'

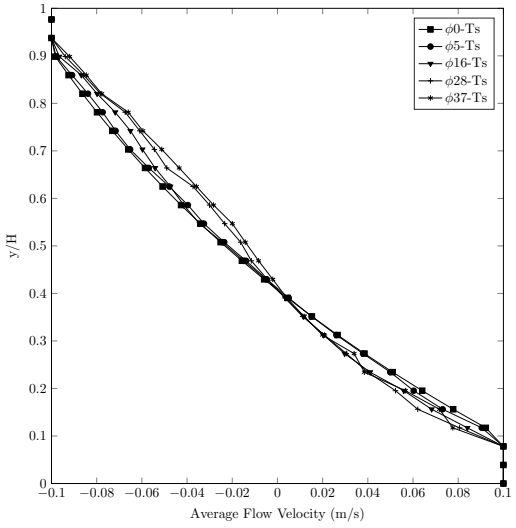

(b) Case 'Ts'

Figure 19: Variation of flow profiles within the different ϕ cases with applied temperature gradient. Note the change in the stationary velocity location away from the centre of the channel, particularly for the lower ϕ cases.

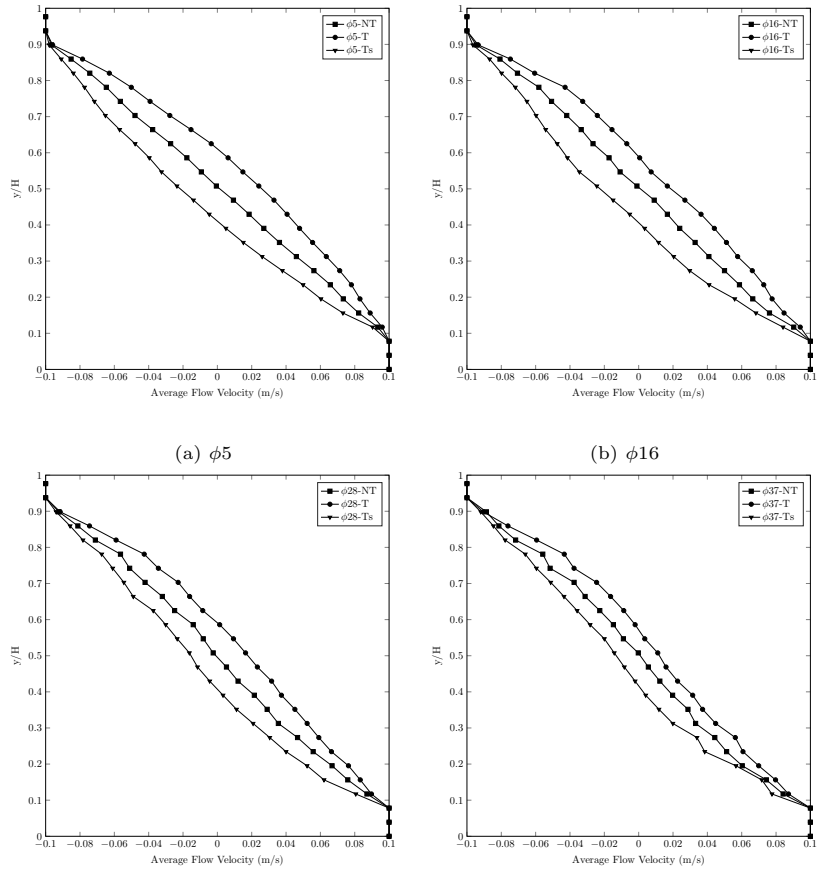

(a) $\phi 5$ (b) $\phi 16$

(c) $\phi 28$ (d) $\phi 37$

Figure 20: Variation of flow profiles within the different temperature cases for the non-zero ϕ cases. Note that as the ϕ increases, the relative impact of the temperature-dependent viscosity variation decreases.

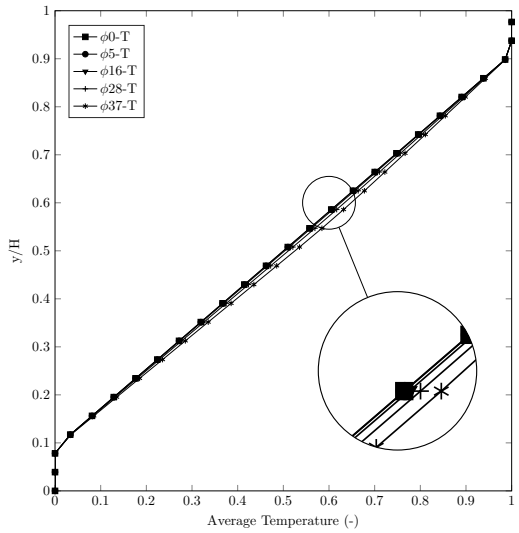

(a) Case 'T'

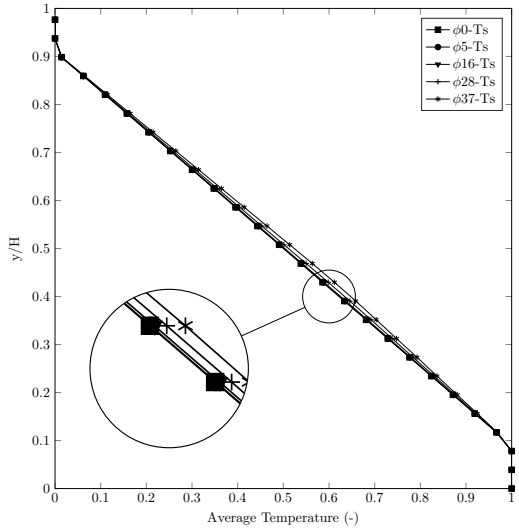

(b) Case 'Ts'

Figure 21: Variation of temperature profiles within the different ϕ cases with applied temperature gradient. The slight increase in temperature is likely due to viscous heating resulting from the effective increase in viscosity with ϕ

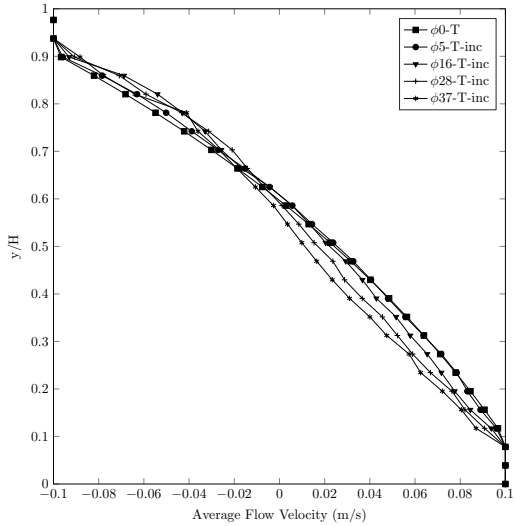

(a) Velocity Case 'T'

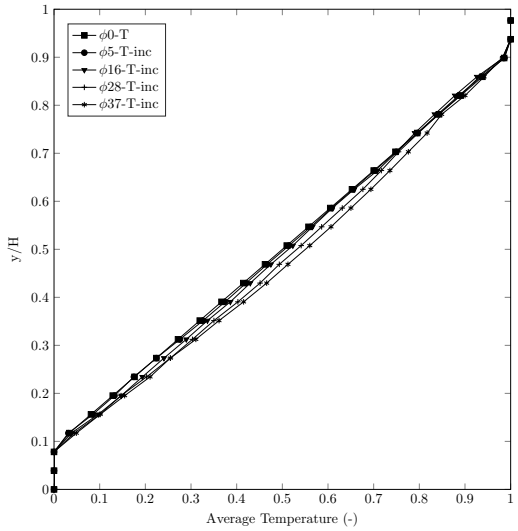

(b) Temperature Case 'T'

Figure 22: Average velocity and temperature profiles of the sheared rheometer test model with the material parameters k and C_p increased by a factor of three over the non-CHT test values.

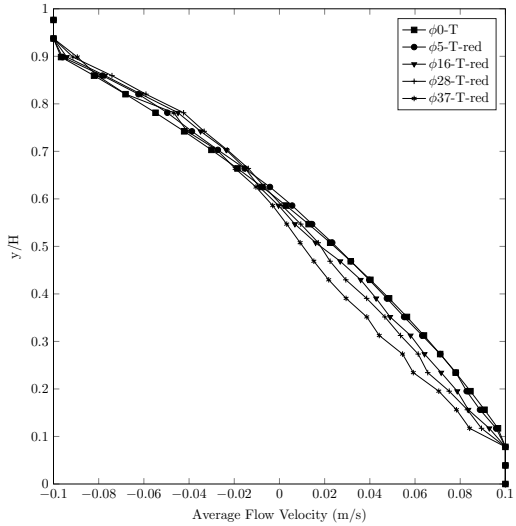

(a) Velocity Case 'T'

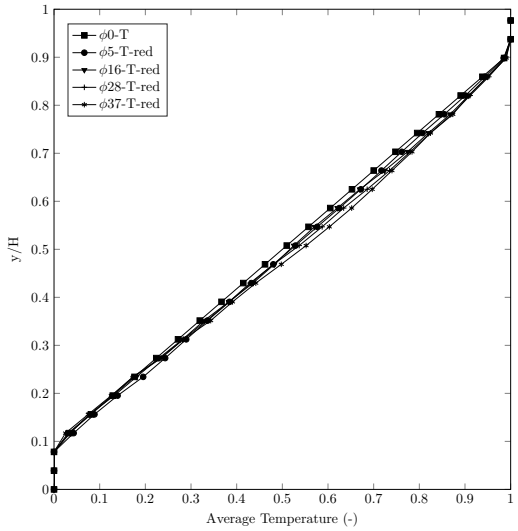

(b) Temperature Case 'T'

Figure 23: Average velocity and temperature profiles of the sheared rheometer test model with the material parameters k and C_p decreased by a factor of three over the non-CHT test values.

Name	**Total Particles**	ϕ
$\phi 0$	120	0%
$\phi 5$	157	5%
$\phi 16$	243	16%
$\phi 28$	337	28%
$\phi 37$	403	37%

Table 1: Solid volume fractions of different test cases examined in a shearing rheometer.

Case	T_{Upper}	T_{Lower}
NT	0	0
T	1	0
Ts	0	1

Table 2: Dimensionless temperature conditions at the walls for numerical rheometry tests.

Property	**non-CHT**	**CHT - increase**	**CHT - decrease**
k	$\frac{1}{6}$	$\frac{1}{2}$	$\frac{1}{18}$
ρC_p	1.0	3.0	$\frac{1}{3}$

Table 3: Thermal material data used for the solid component in the rheometer tests. The fluid component used the non-CHT values in all tests. All values here are in lattice units.